Structural and magnetic study of Sm doped NiFe$_2$O$_4$ nanoparticles

M. Yehia[1] · **A. Hashhash**[1]

Abstract

NiFe$_{2-x}$Sm$_x$O$_4$ ($x = 0.0, 0.01, 0.025, 0.05, 0.075, 0.1$) nanoferrites samples were prepared by sol–gel method. The structural properties of the samples were studied by X-ray powder diffraction, where the formation of a cubic spinel phase was confirmed. The lattice parameter and the particle size were determined by applying Rietveld refinement. A slight change in the lattice parameter was observed for Sm doped nanosamples. Whereas, the particle sizes were found to decrease with increasing Sm concentration (x) and have the highest value (42 nm) for pure NiFe$_2$O$_4$ nanoparticles. The magnetic properties were characterized using Mössbauer effect (ME) spectroscopy and vibrating sample magnetometer (VSM). ME spectroscopy was used to study the distribution of cations in tetrahedral (A) and octahedral [B] sites of the nanoparticles and the degrees of inversion values were obtained. The saturation magnetization, coercivity and remanent magnetization were determined using VSM measurements. These magnetic parameters vary with Sm substitution and found to be mainly affected by the change in the cations distribution and particle sizes.

1 Introduction

Rare earth (R) doped nano-ferrites have been investigated because of their novel physics and chemical properties. These (R) doped nano-ferrites are technologically important materials that are used to produce permanent magnets, electronic and microwave devices, magnetic fluids, spintronics, data storage, magnetic filters, transformers and magnetic switches [1–4]. The magnetic properties of these spinel ferrites are governed by the chemical composition and the method of preparation [5–7]. In the case of nickel ferrites, altering the chemical composition can be achieved by doping with different transition metals and rare earth (R) ions [5, 8].

Not only is the type of the dopant but also its amount is critical in changing the cation distribution and accordingly the physical properties of the doped Ni-ferrite. Using different synthesizing methods could yield different particle sizes, particle size distribution, morphology and cation distribution [8, 9]. There are many preparation methods of nickel ferrite nanocrystals; mechanical milling, sol–gel methods, ceramic method, microwave processing approaches and co-precipitation, microemulsions. Among these methods,

sol–gel process stands as an important method used to obtain ferrite nanoparticles with enhanced homogeneity and controlled particle size in a relatively short processing time and low reaction temperatures.

Single phase NiFe$_{1.99}$R$_{0.01}$O$_4$ (R = Sm, Gd, Eu, La) samples were prepared using the standard ceramic method [8]. Mössbauer effect (ME) measurements suggested that R ions substitute Fe^{3+} ions in the octahedral B site. An increase in the coercivity and saturation magnetization was observed for all doped samples, where the highest saturation magnetization was obtained for Sm-doped Ni-ferrite sample. Then, Zn and Ga doped Ni$_{1-x}$Zn$_x$Fe$_{1.49}$Ga$_{0.5}$Sm$_{0.01}$O$_4$ samples were prepared using the standard ceramic method [10]. Measurements confirmed that Sm^{3+} ions favor the B sites and support magnetism in the studied system, whereas Zn substitution clearly destabilizes the magnetic order and suppresses magnetism in the studied systems. Later, ultrasmall Zn-substituted Ni–Sm–Ga (NiFe$_{1.99}$Sm$_{0.01}$O$_4$ and Ni$_{1-x}$Zn$_x$Fe$_{1.49}$Ga$_{0.5}$Sm$_{0.01}$O$_4$) ferrites nanoparticles were synthesized using sol–gel method [9]. The particle size ranged from D = 4–8 nm, and hence a pronounced superparamagnetism was observed for all the prepared nanoparticles.

In this work, Sm-substituted Ni ferrites NiFe$_{2-x}$Sm$_x$O$_4$ ($x = 0.0, 0.01, 0.025, 0.05, 0.075, 0.1$) were prepared by the sol–gel technique. The influence of Sm^{3+} doping on the structural and magnetic properties of Ni ferrite were systematically studied. The crystal structure was investigated using

✉ M. Yehia
m6yehia@yahoo.com

1 Reactor Physics Department, Nuclear Research Center, Atomic Energy Authority, P. O. Box 13759, Cairo, Egypt

X-ray powder diffraction and Fourier transform-infrared (FTIR), whereas the cation distribution and the magnetic properties were studied using ME spectrometer and vibrating sample magnetometer (VSM).

2 Experimental

$NiFe_{2-x}Sm_xO_4$ ($x=0.0, 0.01, 0.025, 0.05, 0.075, 0.1$) nanoparticles were synthesized using $Fe(NO_3)_3 \cdot 9 H_2O$ [99% Merck, Germany], $Ni(NO_3)_2 \cdot 6H_2O$ [99.9% Strem Chemicals, USA], $Sm(NO_3)_3 \cdot 6H_2O$ [99.9% Strem Chemicals, USA], citric acid ($C_6H_8O_7 \cdot H_2O$) [99.7% Winlab, UK] and distilled water. The structure of the prepared samples was studied at room temperature using X-ray diffraction (XRD) (Philips X'pert multipurpose diffractometer) with CuK_α radiation (with $\lambda = 1.5418$ Å). The crystal structure was refined applying Rietveld profile method using the Rex software [11]. The crystallographic parameters: lattice constant (a), ionic radius per molecule of the tetrahedral and octahedral sites (r_A, r_B), bond length in the two crystallographic sites (R_A and R_B) and oxygen position parameter (u) have been calculated. Jasco FT-IR 310 spectrophotometer were used to carry out FTIR measurements in the frequency range of 2000–250 cm^{-1}. Austin Science Mössbauer Effect Spectrometer with constant acceleration laser-interferometer-controlled drive and data acquisition system is used in a standard transmission setup with a personal Computer Analyzer (PCA II-card with 1024 channel). The radioactive source is ^{57}Co embedded in Rh matrix with initial activity of 50 mCi. Metallic iron spectrum is used for the calibration of both observed velocities and hyperfine magnetic fields. The cation distributions and all (ME) parameters are calculated from the recorded Mössbauer spectra. Magnetic measurements on the synthesized nanoferrites were carried out using VSM (9600-1 LDJ, USA) with a maximum applied field of nearly 20 kG at room temperature and the saturation magnetization M_S and the coercivity H_C were determined.

3 Results and discussion

3.1 XRD measurements

The XRD patterns of $NiFe_{2-x}Sm_xO_4$ ($x=0.0, 0.01, 0.025, 0.05, 0.075, 0.1$) nanoparticles are shown in Fig. 1. For all samples, the observed diffraction peaks can be indexed to $NiFe_2O_4$ with Fd-3m space group. The diffraction patterns exhibit additional impurity peaks of Ni. Using Rex software (Fig. 2), the percentage of Ni phase was calculated and ranged from 3.4% for pure Ni ferrite to <1% for all Sm doped samples. The lattice parameter a_{exp} obtained from the Rietveld refinement of XRD measurements is summarized in Fig. 3b. On the other
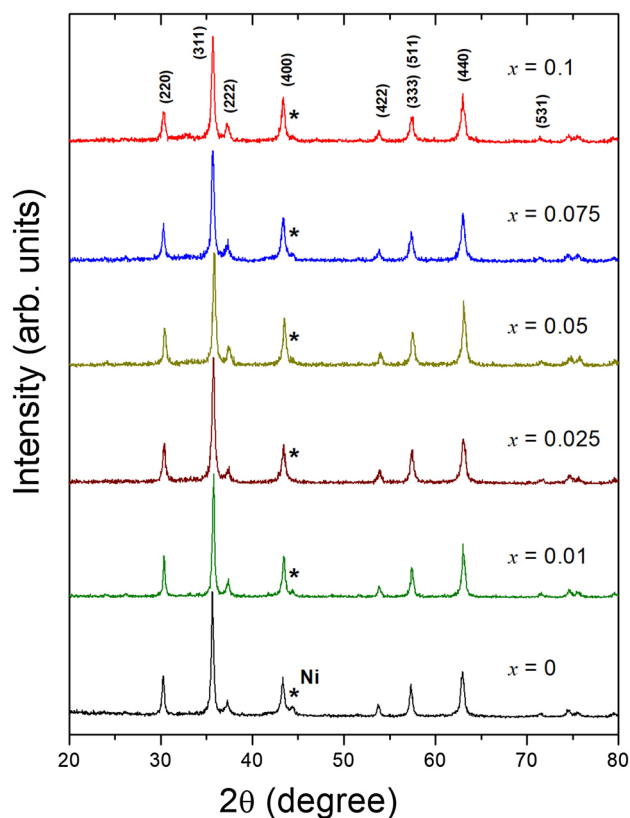

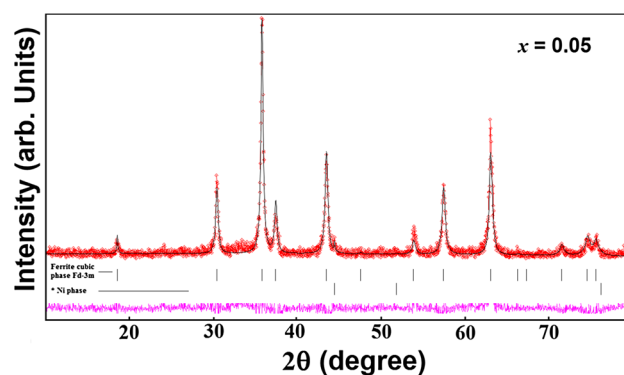**Fig. 1** XRD patterns of different $NiFe_{2-x}Sm_xO_4$ ($x=0.0, 0.01, 0.025, 0.05, 0.075, 0.1$) nanoparticles

Fig. 2 Rietveld refinement profile for $NiFe_{1.95}Sm_{0.05}O_4$ sample

hand, the lattice parameter a_{th} can be theoretically calculated using the cation distribution obtained from ME spectroscopy (Sect. 3.2). The Mean ionic radius per molecule of the A-site (r_A) and B-site (r_B) are given by [12]:

$$r_A = C_{Fe}r(Fe^{3+}) + C_{Ni}r(Ni^{2+}) \tag{1}$$

$$r_B = \frac{1}{2}\left[C_{Fe}r(Fe^{3+}) + C_{Ni}r(Ni^{2+}) + C_{Sm}r(Sm^{3+})\right] \tag{2}$$
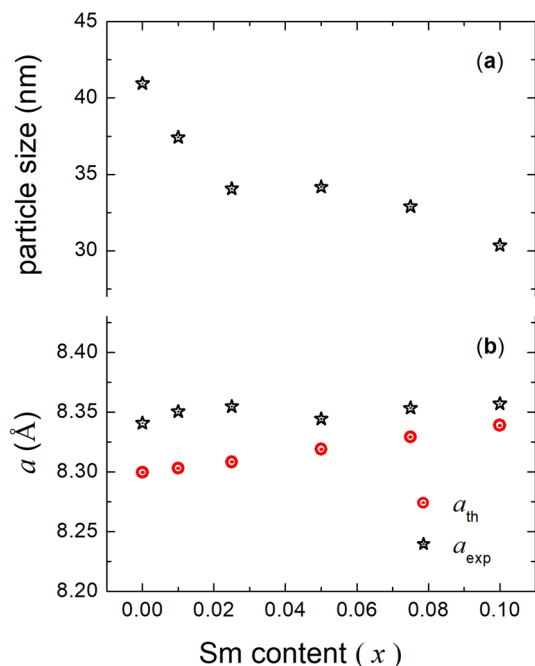
Fig. 3 a Variation of particle size with the substitution of Sm content. **b** Variation of the lattice parameter (*a*) with Sm content *x*. a_{exp} is the lattice parameter obtained from the XRD measurements and a_{th} is the lattice parameter calculated according to the cation distribution obtained from the ME measurements

Table 1 The effective ionic radii of $r(Fe^{3+})$, $r(Ni^{2+})$ and $r(Sm^{3+})$ ions in the tetrahedral A-site and octahedral B-site [13]

Ion	Tetrahedral A-site (Å)	Octahedral B-site (Å)
$r(Fe^{3+})$	0.49	0.645
$r(Ni^{2+})$	0.55	0.69
$r(Sm^{3+})$	–	0.958

where $r(Fe^{3+})$, $r(Ni^{2+})$ and $r(Sm^{3+})$ are the ionic radii of Fe^{3+}, Ni^{2+} and Sm^{3+} ions given in Table 1. The concentration of Fe^{3+}, Ni^{2+} and Sm^{3+} ions in A- and B- sites are C_{Fe}, C_{Ni} and C_{Sm}, respectively and were taken from (ME) results. The average (A–O) and (B–O) bond lengths are R_A and R_B respectively and can be expressed as:

$$R_A = r_A + r_O \tag{3}$$

$$R_B = r_B + r_O \tag{4}$$

where $r_O = 1.32$ Å is the radius of oxygen ion. The lattice parameter a_{th} can be obtained from:

$$a_{th} = \frac{8}{3}\left[(r_A + r_O) + \sqrt{3}(r_B + r_O)\right] \tag{5}$$

The calculated values of a_{th}, r_A, r_B, R_A, R_B and u are illustrated in Table 2. The comparison between the calculated lattice parameter a_{th} and the experimentally obtained a_{exp} are shown in Fig. 3b. According to the ME measurements (Sect. 3.3), nano $NiFe_2O_4$ is a partial inverse spinel, where most of the Ni^{2+} ions set on the B-site, while a small fraction (~9%) enters the A-site. By increasing *x*, Sm^{3+} ions have a clear preference to inter the B-site and gradually substitute Fe^{3+} ions. This process is accompanied by the migration of the Ni^{2+} from the A-site to the B-site. The ionic radius $r(Sm^{3+})$ is bigger than both $r(Fe^{3+})$ and $r(Ni^{2+})$. This why by increasing *x*, both r_A and R_A slightly decrease, while r_B and R_B increase monotonically. The resultant effect is an increase in the lattice parameter. The values of the lattice parameter are very close to the values observed for the bulk Ni ferrite sample [4]. For the A-site, center of symmetry is at $\left(\frac{3}{8}\frac{3}{8}\frac{3}{8}\right)$ and the ideal value of the oxygen positional parameter (u^{43m}) is 0.375. While, the center of symmetry for the B-site is at $\left(\frac{1}{4}\frac{1}{4}\frac{1}{4}\right)$ and the ideal value of u^{3m} is 0.25. In this case, the arrangement of O^{2-} ions correspond exactly to a cubic closed packing. However, in the actual spinel lattice a small deformation from this ideal pattern is observed. As shown in Table 2, the values of u^{3m} and u^{43m} are higher than the ideal values, which indicate that O^{2-} ions move away from the tetrahedrally coordinated A-site cation along the $\langle 111 \rangle$ directions due to the contraction of the tetrahedral interstices, correspondingly the octahedral B-sites become smaller [9]. Such changes in the oxygen positional parameter will affect the A–A interactions and B–B magnetic interactions.

The particle size of $NiFe_{2-x}Sm_xO_4$ nanoparticles can be obtained from the Rietveld refinement of XRD measurements. The broad diffraction peaks observed for all the samples reflect the reduced particle size. The particle size
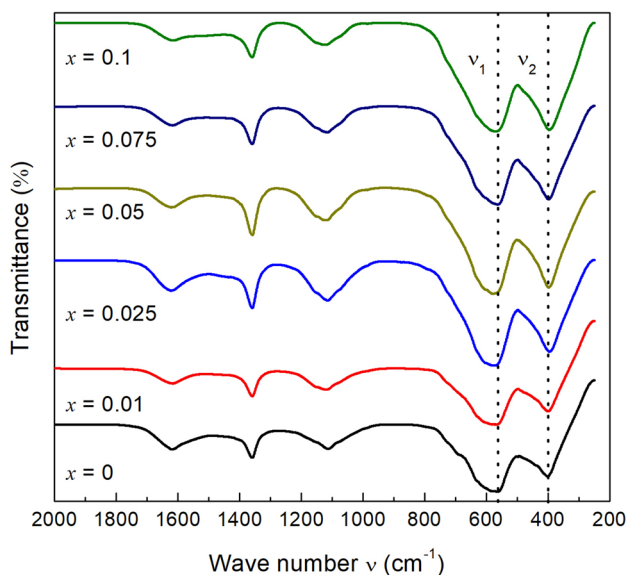
Table 2 Experimental (a_{exp}) and theoretical (a_{th}) lattice constants, ionic radii of A- and B-sites (r_A and r_B), the average bond lengths (R_A and R_B) and the oxygen positional parameter (u) of $NiFe_{2-x}Sm_xO_4$ (x=0.0, 0.01, 0.025, 0.05, 0.075, 0.1) nanoparticles

x	a_{exp} (Å)	a_{th} (Å)	r_A (Å)	R_A (Å)	r_B (Å)	R_B (Å)	u^{3m} (Å)	u^{43m} (Å)
0	8.341	8.2997	0.4951	1.8651	0.6656	2.0356	0.271	0.396
0.01	8.351	8.3032	0.49379	1.8638	0.6676	2.0376	0.2712	0.396
0.025	8.355	8.3084	0.49178	1.8618	0.6707	2.0407	0.2704	0.395
0.05	8.344	8.3191	0.49222	1.8622	0.6745	2.0445	0.2696	0.395
0.075	8.353	8.3292	0.49169	1.8617	0.6786	2.0486	0.2698	0.395
0.1	8.357	8.339	0.49051	1.8605	0.683	2.053	0.2689	0.394

D are shown in Fig. 3, where it varies from ~42 nm for pure Ni-ferrite to ~30 nm for $NiFe_{1.9}Sm_{0.1}O_4$. Generally, by increasing the Sm content x, the particle size decreases. A similar behavior was observed for Nd^{3+} substituted nano Mg–Cd ferrites [14, 15].

3.2 FTIR analysis

FTIR spectra of $NiFe_{2-x}Sm_xO_4$ (x = 0.0, 0.01, 0.025, 0.05, 0.075, 0.1) nanoferrites are shown in Fig. 4 and the vibration frequencies of all the samples are listed in Table 3. Spinel ferrites generally are branded with two vibrational frequency bands, υ_1 around 600–500 cm^{-1} which is related to the Fe^{3+}–O^{2-} and Ni^{2+}–O^{2-} complexes at the tetrahedral site (A) and vibrational frequency υ_2 around 450–350 cm^{-1} which is related to the Fe^{3+}–O^{2-}, Sm^{3+}–O^{2-} and Ni^{2+}–O^{2-} complexes at octahedral (B) site [16]. The differences in vibration frequencies between the two crystallographic A and B-sites are attributed to the differences in bond length between the two sites, where the ionic radius of A-site is smaller than B-site. In this case, the change in values of υ_1 and υ_2 with increasing Sm content reflects the change in bond lengths of Fe^{3+}, Sm^{3+} and Ni^{2+} metal ions complexes present in this ferrite. As discussed before in Sect. 3.1, XRD measurements suggest a slight change in the average bond length R_A, R_B and the lattice parameter a. Accordingly, a minor change in the vibrational frequency υ_1 and υ_2 was observed. The bands at 1613 cm^{-1}, 1359 cm^{-1} and 1115 cm^{-1} are attributed to; (a) the stretching vibration in the residual H–O–H modes of water molecules, (b) the symmetric stretching of the carboxyl group (COOH) and (c) the asymmetric stretching

Table 3 Tetrahedral and octahedral vibrational frequencies (υ_1 and υ_2) of $NiFe_{2-x}Sm_xO_4$ (x = 0.0, 0.01, 0.025, 0.05, 0.075, 0.1) nanoparticles

x	υ_1 (cm^{-1})	υ_2 (cm^{-1})
0	565	397
0.01	580	400
0.025	579	396
0.05	578	397
0.075	563	398
0.1	567	396

vibration of the adsorbed NO_3 produced as a residue from the nitrate group after the combustion of the samples [17].

3.3 ME measurements

Figure 5 shows the room temperature transmission ME spectra of $NiFe_{2-x}Sm_xO_4$ (x = 0.0, 0.01, 0.025, 0.05, 0.075, 0.1). ME spectra spot the hyperfine interactions between the nucleus and its neighboring electrons. There are three main hyperfine interactions, one originates from the electron density at the nucleus (Isomer shift δ), the other from the gradient of the electric field at the nucleus (Quadrupole splitting ΔE_Q), and finally from the unpaired electron density at the nucleus (Hyperfine field H_f). The spectra of all samples were fitted with two magnetic sextets and a paramagnetic doublet. All the fitting parameters are summarized in Table 4. The magnetic sextets are a direct proof of the magnetic order in the studied samples. The existence of two sextets is typical for inverse and partially inverse spinel ferrites, where they

Fig. 4 FTIR spectra of different $NiFe_{2-x}Sm_xO_4$ (x = 0.0, 0.01, 0.025, 0.05, 0.075, 0.1) nanoparticles
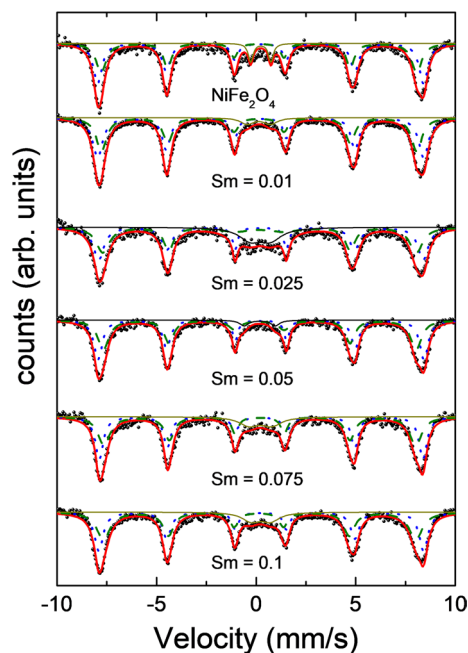
Fig. 5 Room temperature ME spectra of different $NiFe_{2-x}Sm_xO_4$ (x = 0.0, 0.01, 0.025, 0.05, 0.075, 0.1) nanoparticles

Table 4 The isomer shift (δ), quadrupole splitting (ΔE_Q), Hyperfine field (H_f) and the doublet linewidth ω_d of different $NiFe_{2-x}Sm_xO_4$ ($x=0.0$, 0.01, 0.025, 0.05, 0.075, 0.1) nanoparticles
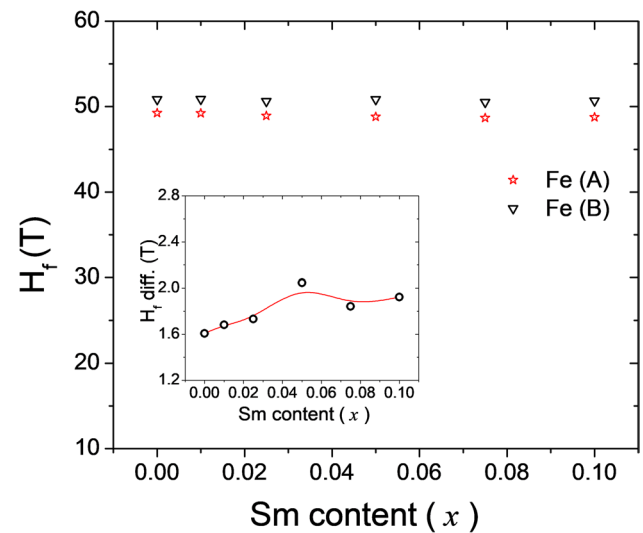
		Sample					
		0	0.01	0.025	0.05	0.075	0.1
δ_A	(mm/s)	0.1402	0.1461	0.1663	0.1745	0.1817	0.151
δ_B	(mm/s)	0.2199	0.2242	0.2359	0.2411	0.2467	0.2427
ΔE_{QA}	(mm/s)	0.0011	0.0016	0.0051	0.0107	0.0149	0.0382
ΔE_{QB}	(mm/s)	0.0019	0.0035	0.0097	0.0031	0.0072	0.0135
H_{fA}	(T)	49.254	49.2087	48.9165	48.8219	48.6768	48.7667
H_{fB}	(T)	50.8608	50.891	50.6492	50.8678	50.5192	50.6907
Doublet							
δ_d	(mm/s)	0.2331	0.2172	0.2068	0.1755	0.21	0.2343
ΔE_{Qd}	(mm/s)	1.0147	1.1779	1.0194	1.5628	1.1412	0.9733
ω_d	(mm/s)	0.2945	0.7927	1.3403	0.521	1.1822	1.1008
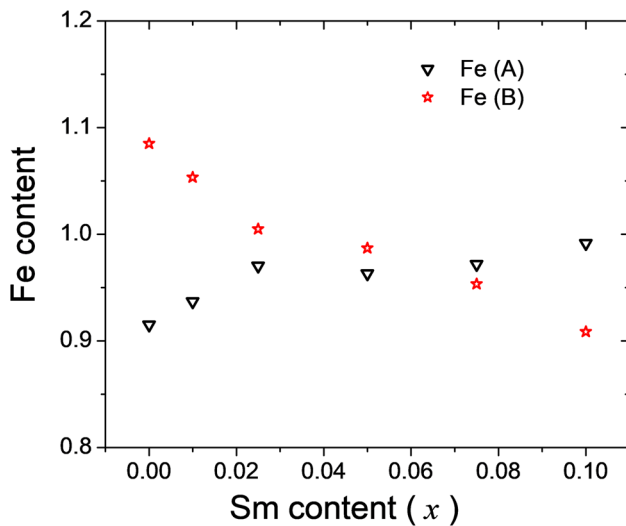
Fig. 6 Fe content calculated from ME spectra for different $NiFe_{2-x}Sm_xO_4$ ($x=0.0$, 0.01, 0.025, 0.05, 0.075, 0.1) nanoparticles

Fig. 7 Mössbauer hyperfine field of different $NiFe_{2-x}Sm_xO_4$ ($x=0.0$, 0.01, 0.025, 0.05, 0.075, 0.1) nanoparticles

refer to Fe^{3+} in both tetrahedral and octahedral environments. For this reason, the area of these two sextets are used for the determination of Fe amount in the A- and B-sites. The sextets attributed to the Fe^{3+} ions at the octahedral (B) have a larger isomer shift and hyperfine field [18]. As presented in Fig. 6, the Fe^{3+} amount in the B-site is slightly higher than that in the A-site, which straight forwardly refers that a portion Ni^{2+} ions set on A-site (~9%). This unusual partial inverse Ni ferrite is due to the reduced particle size [4]. For $x=0.01$, Sm^{3+} ions replace Fe^{3+} in the B-site and in the same time some of the Ni^{2+} ions transfer from the A- to the B-site. By increasing the Sm content x, the behavior continues and the amount of Fe^{3+} ions in the A-site exceed that in the B-site for $x > 0.05$.

In addition to the two sextets components, the spectra of all samples have doublets due to the presence of nano-sized ferrite crystallites below the single domain size (D_{sp}) with superparamagnetic behavior [4, 19]. The area of the

doublets is ranging from (3.58–16.24%). δ values are typical for Fe^{3+} ions in octahedral and tetrahedral environment [4, 5]. Since, the s-electrons charge density of the Fe^{3+} ions is not influenced by crystalline size, the observed values of the isomer shift show a weak change with decreasing D. The quadrupole splitting (ΔE_Q) has values close to zero for both (A)- and [B]-sites.

Figure 7 presents the hyperfine field (H_{fA} and H_{fB}) for both A- and B-sites. Generally, the hyperfine field reflects the internal magnetic field produced by the magnetic ordering on Fe^{3+} ions on both sites. This field is strongly affected by intersite A–A and B–B interactions and the interasites A–B interactions. As the cation distribution changes due to the Sm^{3+} doping, these magnetic interactions change and consequently affect both hyperfine fields. Also, the hyperfine field is sensitive to the decreased particle size, where decreasing the particle size tends to decrease the hyperfine field [20, 21]. Figure 7 suggests that increasing Sm^{3+}

concentration slightly changes H_{fA} and H_{fB}. Generally, for $x \leq 0.1$, Sm^{3+} ions has a minor effect on the magnetic interactions and magnetic order. However, the changes in the cation distribution due to Sm doping is reflected in the difference between H_{fB} and H_{fA}. The difference between H_{fB} and H_{fA} increases gradually by introducing Sm^{3+} ions and it peaks at $x = 0.05$ and then decreases again for higher concentration ($x > 0.05$) where the Fe^{3+} in the A-site exceeds that in the B-site. The change in the cation distribution can also be spotted in the doublets parameters. As indicated in Fig. 8, pronounced differences are observed in the behavior of δ_d, ΔE_{Qd} and doublet linewidth ω_d for $x < 0.05$ and $x > 0.05$. Such behavior can be attributed to the changes in the A–B interactions due to partial transfer of the Fe^{3+} ions from the B-site to the A-site by increasing Sm^{3+} concentration.

3.4 Magnetic properties

Figure 9 shows the variation of magnetization as a function of the applied magnetic field for various $NiFe_{2-x}Sm_xO_4$ ($x = 0.0, 0.01, 0.025, 0.05, 0.075, 0.1$) nanoparticles at 300 K. The M–H curve provides information regarding the
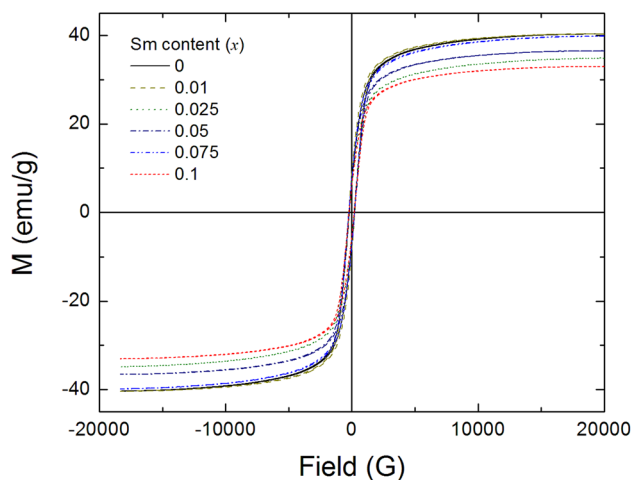
Fig. 9 VSM measurements for $NiFe_{2-x}Sm_xO_4$ ($x=0.0$, 0.01, 0.025, 0.05, 0.075, 0.1) nanoparticles

magnetic parameters such as saturation magnetization (M_S), coercivity (H_c) and remanent magnetization (Mr), which are summarized in Table 5. Saturation magnetization (M_S) and

Fig. 8 For different nanoparticles **a** Isomer shift of the paramagnetic doublet. **b** Quadrapole splitting of the paramagnetic doublet. **c** Linewidth of the paramagnetic doublet
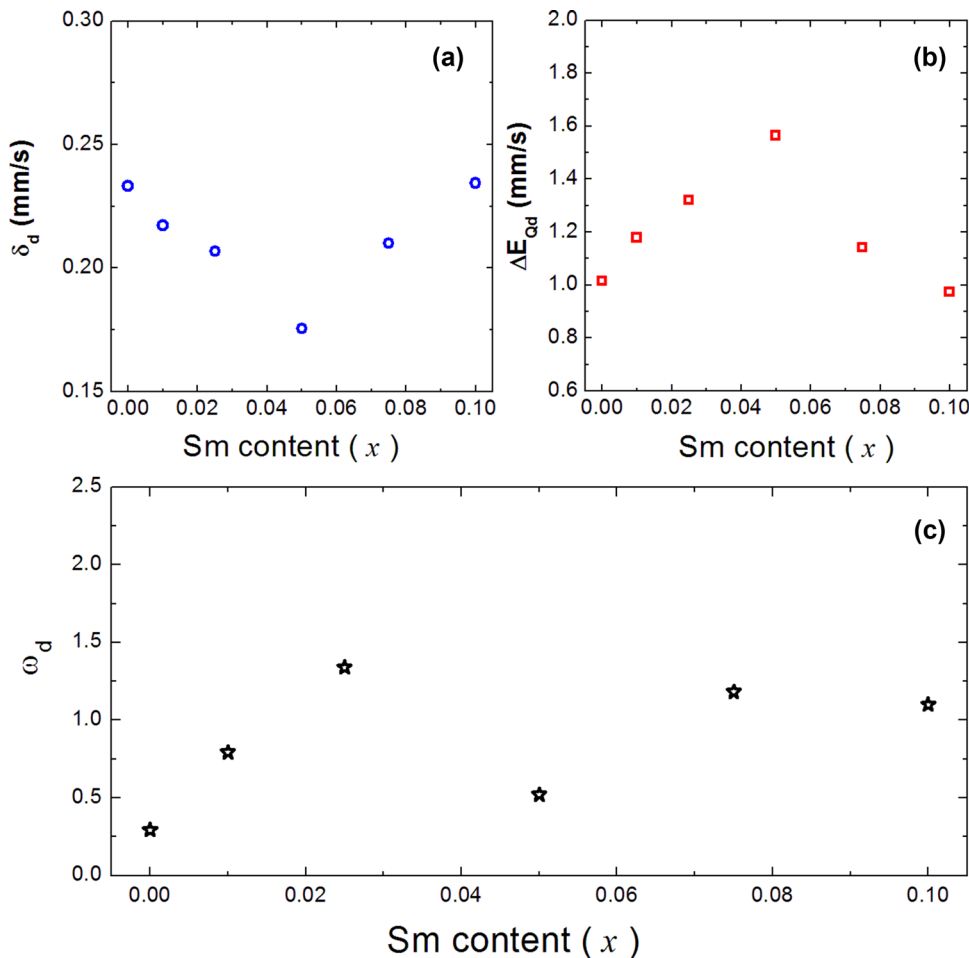
Coercivity (H_c) are shown in Fig. 10. Generally, the magnetic properties should mainly depend on Sm^{3+} content and the cation distribution of different ions between A and B sites. However, the magnetic properties of nanoferrites also strongly depend on the particle size and the particle size distribution. The saturation magnetization (M_S) is expected to decrease with decreasing the particle size [4]. The magnetic moment per formula unit in Bohr magneton (μ_B) can be calculated using the relation [8]:

$$M_{obs} = \frac{(\text{saturation magnetization}) \times (\text{molecular weight})}{5585}$$

(6)

The value of M_{obs} is presented in Table 4 and Fig. 10a. The magnetic properties of ferrites are mainly governed by super exchange interactions and therefore changing the cation distribution and introducing rare earth Sm would affect A–A, A–B and B–B magnetic interactions. According to Néel's theory, the magnetic moment M_{cal} is expressed as:

$$M_{cal} = M_B - M_A$$

(7)

The concentration of different ions in the A- and B-sites are obtained from the ME measurements and the magnetic moment of Ni^{2+}, Fe^{3+} and Sm^{3+} ions are 2 μ_B, 5 μ_B and 5 μ_B, respectively. The dashed line is the expected value for complete inverse $NiFe_2O_4$, which is exact 2 μ_B. For all the samples, M_{cal} values are significantly higher than the observed values. M_S value depends on the ions magnetic moments, and the distance and angle between two adjacent magnetic ions. The larger ionic radii of Sm^{3+} ions compared to Fe^{3+} ions causes changes in the lattice parameter, bond lengths, bond angles and oxygen positional parameter, which would lead to the variation of the magnetic interactions. Moreover, the change in the cation distribution will also affect the magnetic interactions. Finally, the reduced particle size of the prepared nanoparticles decreases M_S values [3, 22, 23]. The coercivity of the ferrites nanoparticles depends on internal micro stress
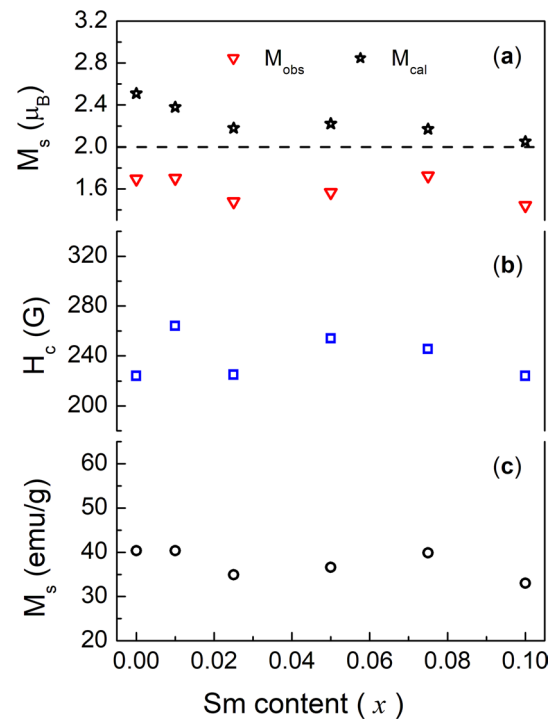
Fig. 10 a Comparison between observed magnetic moment obtained from VSM measurements (M_{obs}) and calculated magnetic moments according to Néel's theory (M_{cal}). **b** Coercivity (H_c) and **c** Saturation magnetization (M_S) for $NiFe_{2-x}Sm_xO_4$ ($x=0.0, 0.01, 0.025, 0.05, 0.075, 0.1$) nanoparticles

due to distortion of lattice, different electronic configuration of the ions and particle size. Sm^{3+} ions concentration would logically affect H_C since Sm^{3+} 4f electrons have a strong spin–orbit coupling [22]. The change in coercivity with Sm^{3+} ions concentration can be attributed to the decrease in particle size and the changes in the cation distribution. The squareness $R^2 = M_R/M_S$ for all the studied samples is ranging from 0.235–0.314. Since the squareness is smaller than 0.5, $NiFe_{2-x}Sm_xO_4$ nanoparticles would have uniaxial anisotropy which arises due to surface effect [23, 24].

Table 5 Saturation magnitization (M_S), Coercivity (H_C), Remanent magnetization (M_r), Squareness ration (R^2), observed magnetic moment (M_{obs}) and calculated magnetic moments according to Néel's theory (M_{cal}) for $NiFe_{2-x}Sm_xO_4$ ($x=0.0, 0.01, 0.025, 0.05, 0.075, 0.1$) nanoparticles

x	M_S (emu/g)	H_C (G)	M_r	R^2	M_{obs} (μ_B)	M_{cal} (μ_B)
0	40.372	224.07	9.49	0.235	1.69425	2.51
0.01	40.37	264.07	12.7	0.314	1.70099	2.38
0.025	34.901	225.09	8.35	0.239	1.47942	2.18
0.05	36.589	254.1	10.56	0.289	1.56645	2.22
0.075	39.898	245.58	10.73	0.269	1.72499	2.17
0.1	33.035	224.01	7.93	0.24	1.44225	2.05

4 Conclusion

$NiFe_{2-x}Sm_xO_4$ ($x = 0.0$, 0.01, 0.025, 0.05, 0.075, 0.1) nanocrystalline ferrites were synthesized by sol–gel technique. The structural parameters; lattice parameter (a), bond lengths and oxygen positional parameter (u) were calculated from the X-ray powder diffraction measurements. These structure parameters vary systemically with the substitution of Sm^{3+} ions. ME spectroscopy was utilized to study the magnetic properties and determine the cation distribution. For all the samples, ME spectra contain two magnetic sextets and a paramagnetic doublet, which suggest the coexistence of the magnetic order for large particle sizes and superparamagnetic behavior for small particle sizes below D_{sp}. The saturation magnitization (M_S), coercivity (H_C) and remanent magnetization (M_r) were determined from the VSM measurements. The squareness ratio suggests that all the studied nanoparticles have uniaxial anisotropy. The observed magnetic moment values (M_{obs}) for all samples are significantly lower than the calculated magnetic moments according to Néel's theory (M_{cal}). These reduced values of M_{obs} can be attributed to the reduced particle sizes of the prepared nanoferrites.

References

1. K.V. Zipare, S.S. Bandgar, G.S. Shahane, J. Rare Earths **36**, 86–94 (2018)
2. S. Ikram, M.I. Arshad, K. Mahmood, A. Ali, N. Amin, N. Ali, J. Alloys Compd. **769**, 1019–1025 (2018)
3. M.N. Akhtar, A.B. Sulong, M.N. Akhtar, M.A. Khan, J. Rare Earths **36**, 156–164 (2018)
4. M. Yehia, Sh Labib, S.M. Ismail, Phys. B **446**, 49–54 (2014)
5. A. Hashhash, M. Yehia, S.M. Ismail, S.S. Ata-Allah, J. Supercond. Nov. Magn. **27**, 2305–2310 (2014)
6. M. Rahimi-Nasrabadi, M. Behpour, A. Sobhani-Nasab, M.R. Jeddy, J. Mater. Sci.: Mater. Electron. **27**, 11691–11697 (2016)
7. M. Rahimi-Nasrabadi, M. Behpour, A. Sobhani-Nasab, S.M. Hosseinpour-Mashkani, J. Mater. Sci.: Mater. Electron. **26**, 9776–9781 (2015)
8. M. Yehia, S.M. Ismail, A. Hashhash, J. Supercond. Nov. Magn. **27**, 771–774 (2014)
9. M. Yehia, S.M. Ismail, M.B. Mohamed, J. Supercond. Nov. Magn. **28**, 3335–3342 (2015)
10. S.M. Ismail, M. Yehia, S.S. Ata-Allah, J. Supercond. Nov. Magn. **28**, 2875 (2004)
11. M. Bortolotti, I. Lonardelli, J. Appl. Cryst. **46**, 259–261 (2013)
12. V.K. Lakhani, T.K. Pathak, N.H. Vasoya, K.B. Modi, Solid State Sci. **13**, 539–547 (2011)
13. A. Dean John, *Lange's Handbook of Chemistry* (McGraw-Hill, New York, 1999)
14. S.R. Bhongale, H.R. Ingawale, T.J. Shinde, P.N. Vasambekar, J. Rare Earths **36**, 390–397 (2018)
15. M. Tsvetkov, M. Milanova, I. Ivanova, D. Neov, Z. Cherkezova-Zheleva, J. Zaharieva, M. Abrashev, J. Mol. Struct. (2019). https://doi.org/10.1016/j.molstruc.2018.07.083
16. M. Deepty, Ch Srinivas, E.R. Kumar, N.K. Mohan, C.L. Prajapat, T.C. Rao, S.S. Meena, A.K. Verma, D.L. Sastry, Ceram. Int. (2019). https://doi.org/10.1016/j.ceramint.2019.01.029
17. A. Hashhash, M. Kaiser, J. Electron. Mater. **45**, 462–472 (2016)
18. K.M. Srinivasamurthy, V.J. Angadi, S.P. Kubrin, S. Matteppanavar, P.M. Kumar, B. Rudraswamy, Ceram. Int. **44**, 18878–18885 (2018)
19. S. Joshi, M. Kumar, H. Pandey, M. Singh, P. Pal, J. Alloys Compd. **768**, 287–297 (2018)
20. S. Mørup, M.F. Hansen, C. Frandsen, Beilstein J. Nanotechnol. **1**, 182–190 (2010)
21. S. Mørup, M.F. Hansen, C. Frandsen, Beilstein J. Nanotechnol. **1**, 48–54 (2010)
22. S.I. Ahmad, S.A. Ansari, D.R Kumar, Mater. Chem. Phys. 208, 248–257 (2018)
23. A. Pathania, S. Bhardwaj, S.S. Thakur, J.L. Mattei, P. Queffelec, L.V. Panina, P. Thakur, A. Thakur, Phys. B **531**, 45–50 (2018)
24. T. Vigneswari, P. Raji, J. Mol. Struct. **1127**, 515–521 (2017)